Chemical Science

ROYAL SOCIETY OF CHEMISTRY

EDGE ARTICLE

View Article Online
View Journal | View Issue

Cite this: *Chem. Sci.*, 2021, **12**, 2108

All publication charges for this article have been paid for by the Royal Society of Chemistry

Received 26th September 2020
Accepted 10th December 2020

DOI: 10.1039/d0sc05340f

rsc.li/chemical-science

Fast oxygen ion migration in Cu–In–oxide bulk and its utilization for effective CO_2 conversion at lower temperature†

Jun-Ichiro Makiura,[a] Takuma Higo,[a]* Yutaro Kurosawa,[a] Kota Murakami,[a] Shuhei Ogo,[a] Hideaki Tsuneki,[a] Yasushi Hashimoto,[a] Yasushi Sato[b] and Yasushi Sekine[a]*

Efficient activation of CO_2 at low temperature was achieved by reverse water–gas shift *via* chemical looping (RWGS-CL) by virtue of fast oxygen ion migration in a Cu–In structured oxide, even at lower temperatures. Results show that a novel Cu–In_2O_3 structured oxide can show a remarkably higher CO_2 splitting rate than ever reported. Various analyses revealed that RWGS-CL on Cu–In_2O_3 is derived from redox between Cu–In_2O_3 and Cu–In alloy. Key factors for high CO_2 splitting rate were fast migration of oxide ions in the alloy and the preferential oxidation of the interface of alloy–In_2O_3 in the bulk of the particles. The findings reported herein can open up new avenues to achieve effective CO_2 conversion at lower temperatures.

Introduction

Anthropogenic emissions of greenhouse gases are regarded as a cause of global warming, which is expected to lead to severe future climate change. Particularly, carbon dioxide (CO_2) derived from fossil fuels and industrial processes has long presented strong effects that continue to raise global mean temperatures.[1,2] Therefore, development of CO_2 capture and utilization (CCU) technologies[2–9] represents an urgent task for reducing CO_2 emissions into the atmosphere and for establishing a sustainable carbon cycle. Synthesis of fuels using electricity generation from renewable resources and using CO_2, most notably sun-to-fuel (STF)[5] and power-to-liquid[6] processes, has been proposed as a means of developing CCU technologies. In fact, CO_2-based fuels are anticipated as a technology that can increasingly incorporate renewable energy into the mobility sector as an "e-fuel".[8,9] For these fuel production technologies, the potential process route is a Fischer–Tropsch (FT) process using syngas, which includes hydrogen and carbon monoxide (CO) converted from captured CO_2.[2–4] As a method of efficient conversion of CO_2 to CO through this process, reverse water–gas shift (RWGS) is a promising reaction that uses renewable H_2.[10,11] Mallapragada *et al.* proposed that the STF route consisting of RWGS followed by the FT reaction has higher efficiency than other routes with direct CO_2 conversion by photosynthetic bacteria and biomass conversion.[5] The RWGS is an equilibrium-limited reaction (eqn (1)) with an endothermic nature.

$$CO_2 + H_2 \leftrightarrow CO + H_2O,\ \Delta H^0_{298} = 42.1\ \text{kJ mol}^{-1} \quad (1)$$

This reaction requires high reaction temperatures and separation of gas products to gain high conversion and a suitable H_2/CO ratio in syngas. Furthermore, conventional catalytic RWGS processes include side reactions, as presented in eqn (2) and (3).

$$CO + 3H_2 \leftrightarrow CH_4 + H_2O,\ \Delta H^0_{298} = -206.5\ \text{kJ mol}^{-1} \quad (2)$$

$$CO_2 + 4H_2 \leftrightarrow CH_4 + 2H_2O,\ \Delta H^0_{298} = -165.0\ \text{kJ mol}^{-1} \quad (3)$$

The CH_4 produced *via* these side reactions makes gas separation more complex. Additionally, it loses energy because of the exothermic reaction. S.-C. Yang *et al.* reported a Cu/CeO_x catalyst[12] which demonstrates 100% CO selectivity at 573 K. However, at low temperatures, CO_2 conversion is low because RWGS is an equilibrium-limited endothermic reaction, which results in a much higher H_2/CO ratio of the obtained syngas than the suitable ratio (H_2/CO = 2) for fuel synthesis by the FT process. One solution for these shortcomings is using chemical-looping reverse water–gas shift (RWGS-CL).[13,14] The overall concept of the solar-driven fuel (chemical) synthesis process with RWGS-CL is presented in Fig. 1. Through this process, CO_2 is converted to CO in two separate steps: reduction and re-oxidation of a metal oxide as an oxygen storage material (OSM). First, the OSM is reduced by H_2 (reaction (4)). Subsequently, the reduced OSM is re-oxidized by CO_2 to generate pure CO (reaction (5)).

[a]*Department of Applied Chemistry, Waseda University, Tokyo 169-8555, Japan. E-mail: t-higo@aoni.waseda.jp; ysekine@waseda.jp*

[b]*ENEOS, 1-1-2 Otemachi, Chiyoda, Tokyo 100 8162, Japan*

† Electronic supplementary information (ESI) available: Experimental procedure, supporting data *etc.* See DOI: 10.1039/d0sc05340f

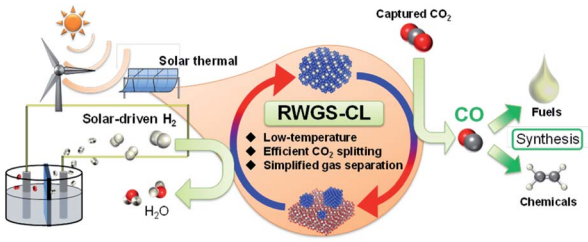

Fig. 1 Concept of solar-driven fuels and chemical synthesis processes with RWGS-CL.

$$MO_x + \delta H_2 \rightarrow MO_{x-\delta} + \delta H_2O \quad (4)$$

$$MO_{x-\delta} + \delta CO_2 \rightarrow MO_x + \delta CO \quad (5)$$

Actually, RWGS-CL has benefits deriving from the absence of undesirable side reactions, which drives the equilibrium to CO production, and simplified gas separation, which leads to its improved energy efficiency. In fact, Wenzel *et al.* investigated solar-to-syngas efficiency for RWGS-CL processes and reported that the energy demand for separation is reduced by 77% compared to conventional RWGS processes.[13] In the RWGS-CL process, the development of the OSM is an indispensable factor to make this process feasible. The rates of reduction and oxidation, CO yield, and stability are emphasized as key factors affecting the OSM for the RWGS-CL cycles. Furthermore, the operation temperature is an important factor. Isothermal operation at lower temperatures is desired to reduce heat loss and to increase its feasibility.[14] In recent years, great effort has been put forth for the development of OSMs with high redox properties for RWGS-CL.[14–19] In previous studies, perovskite-type oxides[14,15] and iron-based oxides[16–18] have been well reported. Perovskite-type oxides are some of the promising OSMs thanks to their high stability and redox properties.[20] Maiti *et al.* investigated a series of lanthanum-based perovskites and found that $LaCa_{0.4}Fe_{0.4}Mn_{0.6}O_3$ showed high CO_2 splitting rate at low temperatures (723–823 K).[15] Iron-based oxides are other candidates of OSMs for RWGS-CL because of their high oxygen capacity. Cu, Co, and Mn co-doped ferrites[16,17] and Fe_2O_3 supported on ion-conductive oxides[18] were developed, which showed high performance and stability for the RWGS-CL cycle at 923 K. However, in these OSMs, isothermal operations have been investigated at temperatures above 823 K, and the performance below 773 K is unclear. Although Utsis *et al.* reported isothermal RWGS-CL at 623–723 K using Fe-substituted Ba-hexa-aluminates,[19] the CO_2 splitting capacity was 0.4 mmol g^{-1}, so higher performance of CO_2 splitting is desired. This study has revealed that an indium-based oxide can be a novel OSM material able to exhibit extremely high isothermal RWGS-CL performance at low temperatures (673–773 K). Particularly, the performance of Cu-modified In_2O_3 formed from $Cu_2In_2O_5$ as a parent material was found to be promising for this purpose. Characterization of OSMs was conducted using powder X-ray diffraction (XRD), a field emission transmission electron microscope equipped with an energy-dispersive X-ray spectrometer (STEM-EDX), X-ray photoelectron spectroscopy (XPS), and *in situ* X-ray absorption fine structure (XAFS) measurements.

Results and discussion

Isothermal RWGS-CL performance

After applying various oxides for RWGS-CL, we found that the Cu–In mixed oxide has high potential for RWGS-CL. The CO_2 splitting performance obtained in this study is presented in Fig. 2 and Table S1† along with results described in earlier reports of the literature. Compared to other perovskite-type oxides[14,15] and ferrites,[16,17] which were reported earlier, Cu–In_2O_3 showed higher CO_2 splitting rates and sufficient amounts of CO_2 splitting even at low temperatures such as 673–773 K. Among all the oxides, Cu–In_2O_3 derived from $Cu_2In_2O_5$ is the most promising material for low-temperature isothermal RWGS-CL. The cycling performance of isothermal RWGS-CL on $Cu_2In_2O_5$ at 773 K is presented in ESI Fig. S1.† The reduction and oxidation (redox) amounts are defined as the moles of oxygen released or restored per gram of $Cu_2In_2O_5$. In the first cycle, $Cu_2In_2O_5$ showed reduction of 9.50 mmol g^{-1} and re-oxidation of 4.82 mmol g^{-1}. Then, in cycles 2–5, the reduction and the oxidation amounts were, respectively, 5.06 ± 0.41 mmol g^{-1} and 4.80 ± 0.40 mmol g^{-1}. Excess reduction in the first cycle (4.68 mmol g^{-1}) was almost equivalent to the release of 2 mol oxygen atoms per mol of $Cu_2In_2O_5$. This finding suggests that $Cu_2In_2O_5$ has become Cu(0)–In_2O_3, which is confirmed later. Products of RWGS-CL were measured using a quadrupole mass spectrometer. The mass spectra of products are presented in ESI Fig. S2.† The products of reduction and oxidation steps were identified, respectively, as H_2O ($m/z = 18$) and CO ($m/z = 28$) without production of other by-products. Results confirmed that RWGS-CL on Cu–In_2O_3 formed from $Cu_2In_2O_5$ is a selective CO_2 conversion to CO. Structural characterization of this material was achieved using a multi-point BET method (results and discussion are presented in ESI Tables S2, S3 and ESI text†), powder XRD, STEM-EDX, and *in situ* XAFS measurements. The XRD patterns obtained from fresh and post-reaction samples are shown in Fig. 3A. The XRD pattern of the fresh sample showed the formation of $Cu_2In_2O_5$ (ICDD 01-070-1082) with no

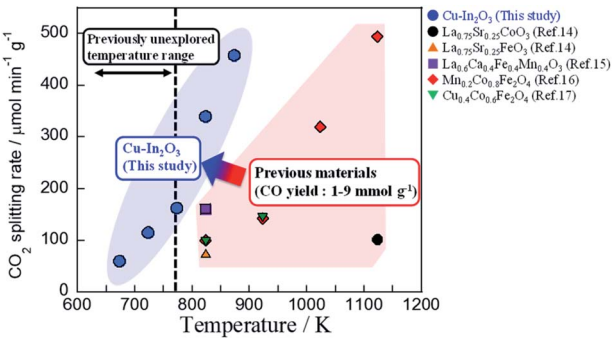

Fig. 2 Average CO_2 splitting rates on the Cu–In mixed oxide (this study) and on various oxides in earlier reports.

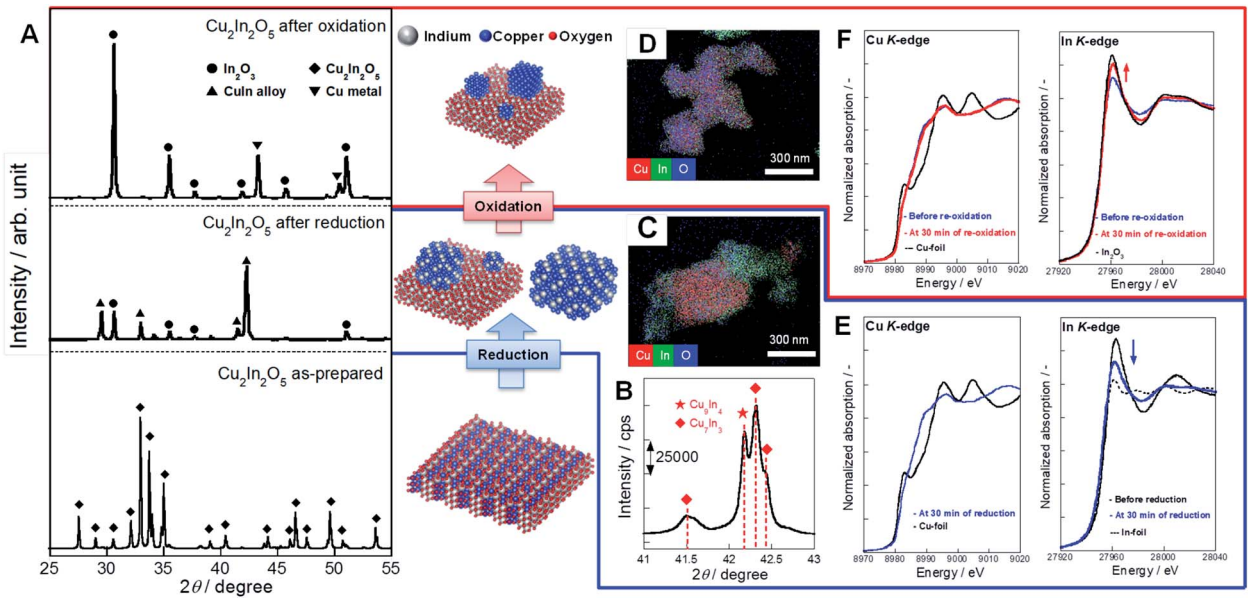

Fig. 3 Structural characterization of Cu–In_2O_3 derived from $Cu_2In_2O_5$ during each step of the RWGS-CL cycle. (A) XRD diffraction patterns of $Cu_2In_2O_5$ as prepared, after reduction, and after oxidation. (B) Main diffraction peaks for the Cu–In alloy on the sample after reduction. EDX image of Cu–In_2O_3 after reduction (C) and re-oxidation (D) at 773 K (copper, red; indium, green; oxygen, blue). Cu and In K-edge XANES spectra of Cu–In_2O_3 during the reduction (E) and the re-oxidation (F).

impurity phase. The XRD pattern of the reduced sample exhibited diffraction peaks assigned to Cu–In alloy and In_2O_3 (ICDD 01-089-4595). The main compositions of the alloy were Cu_7In_3 (ICDD 03-065-2249) and Cu_9In_4 (ICDD 00-042-1476) (Fig. 3B and S3†). From the phase diagram of the Cu–In system, these alloys are considered to be a solid phase during the RWGS-CL cycle.[21] Then, after the oxidation step, diffraction peaks of the Cu–In alloy disappeared. Those of Cu metal (ICDD 01-071-4610) and In_2O_3 were observed. STEM-EDX images are presented in Fig. 3C, D and ESI Fig. S4.† The SEM micrographs of the reduced Cu–In_2O_3 (ESI Fig. S4A†) show the presence of *ca.* 1 μm particles. The elemental composition of the particles was identified using EDX mapping (copper, red; indium, green; oxygen, blue). Results of EDX mapping of the sample after reduction (Fig. 3C and ESI Fig. S4A†) show that indium is distributed evenly over the particles, whereas copper is localized and oxygen is scattered. These images indicate Cu–In alloy formation by reduction. For the re-oxidized sample, many particles with uniformly distributed copper, indium, and oxygen were observed as depicted in Fig. 3D and ESI Fig. S4B.† Using image processing and analysis of these EDX images with Python (see the ESI text and Fig. S5 for details†), it was estimated that 84% of In was overlapping with Cu, and 93% of Cu was overlapping with In. These results demonstrate that a fine matrix of Cu–In–O was formed in the re-oxidized particles. The Cu in re-oxidized particles was regarded as highly distributed on the surface or incorporated into the In_2O_3 structure. As additional information, *in situ* XAFS results are presented in Fig. 3E and F (see the ESI text, Table S4 and Fig. S6–S8 for details†). The sequential change of In K-edge XANES spectra indicates that the redox of In(III) ⇆ In(0) occurs during the RWGS-CL cycle. By contrast, the Cu K-edge XANES spectrum, which only slightly changed during the RWGS-CL cycle, represented the formation of the Cu–In alloy.[22,23] This structural information obtained from XRD, STEM-EDX, and XAFS measurements demonstrates that the RWGS-CL cycle on $Cu_2In_2O_5$, as a parent material, is based on the redox of indium with the formation and oxidation of the Cu–In alloy. This material during RWGS-CL is denoted hereinafter as Cu–In_2O_3.

To elucidate the role of Cu in Cu–In_2O_3, we compared the performance of isothermal RWGS-CL as a function of temperature on Cu–In_2O_3 (derived from $Cu_2In_2O_5$), 10 wt% Cu supported on In_2O_3 (10 wt% Cu/In_2O_3) and pure In_2O_3 without Cu, as shown in Fig. 4. Results indicate that Cu–In_2O_3 is feasible for conducting RWGS-CL, even at 673 K. The performance at each temperature was much higher than that of 10 wt% Cu/In_2O_3 and pure In_2O_3 without Cu. Actually, the amount of redox on 10 wt% Cu/In_2O_3 was slightly higher than that of In_2O_3,

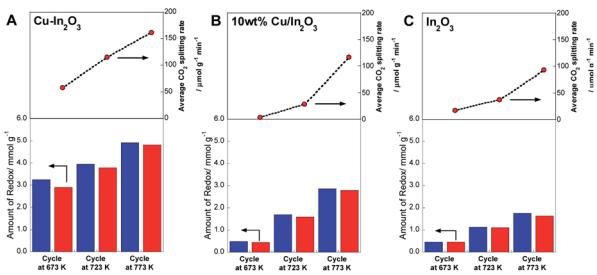

Fig. 4 Dependence of RWGS-CL performance of each oxide on the reaction temperature. Amounts of redox and average CO_2 splitting rate during the re-oxidation step on Cu–In_2O_3 (A), 10 wt% Cu/In_2O_3 (B), and In_2O_3 (C). Reduction was conducted in a 10% H_2 atmosphere for 30 min; oxidation was conducted in a 10% CO_2 atmosphere.

although the CO_2 splitting rate was improved only slightly. Results of structural characterization of 10 wt% Cu/In_2O_3 (ESI text and Fig. S9–S13† provide additional details) show that, because of the poor contact of Cu species with the In_2O_3 surface, 10 wt% Cu/In_2O_3 showed lower performance than Cu–In_2O_3 derived from $Cu_2In_2O_5$.

Kinetics investigations of oxides during the RWGS-CL cycle

Reduction step by H_2. Temperature-programmed reduction by H_2 (H_2-TPR) measurements, the results of which are presented in Fig. 5A, were performed to investigate the reducibility of oxides. The ESI presents additional details.† For Cu-containing oxides (Cu–In_2O_3 and 10 wt% Cu/In_2O_3), the H_2-TPR profiles showed three notable reduction areas (*ca.* 400–550 K, 580–700 K, and 700–920 K). In the moderate temperature region of 580–700 K, the amount of reduction was equivalent to about 26% of oxygen contained in $Cu_2In_2O_5$. Ploner *et al.* have observed that the Cu–In alloy formed at 640–723 K on the Cu–In_2O_3 system in an H_2 atmosphere using *in situ* XRD measurement.[24] Therefore, the reduction of In(III) with the formation of the Cu–In alloy, the composition of which finally approached Cu_9In_4, was regarded as proceeding in this moderate temperature region. Regarding the results of H_2-TPR measurements, results show that Cu species promote the reduction of indium oxide at low temperatures. To investigate more details of the mechanism, the kinetics model for the reduction of these oxides was verified using the method presented by Hancock and Sharp for the isothermal solid-state reaction.[25–27] The ESI text, Fig. S14–S17 and Tables S6–S8† present additional details. The kinetics models used for model fitting are shown in ESI Table S5.† As a result of the investigations, the phase-boundary-controlled reaction models (R2 and R3 models) were found to be suitable to describe the experimentally obtained data for all the oxides. These models are categorized as a classic shrinking core model in which the rate-controlling step is the surface chemical reaction.[26,27] The activation energy was investigated using the reaction rate constant k values obtained from the model fitting described above (ESI Table S9†). Plots of ln (k_{red}/min^{-1}) *vs.* $1/T$ (Arrhenius plot) for the three oxides are presented in Fig. 5B. The respective activation energies for Cu–In_2O_3 (45.2 kJ mol^{-1}) and 10 wt% Cu/In_2O_3 (53.4 kJ mol^{-1}) were much lower than that for In_2O_3 (76.6 kJ mol^{-1}), confirming that the Cu species supported on In_2O_3 decreased the activation barrier for reactions between the surfaces of In_2O_3 and H_2. The slight difference in the activation energy between Cu–In_2O_3 and 10 wt% Cu/In_2O_3 suggests that the effect of the Cu species on the reduction does not depend much on these morphologies.

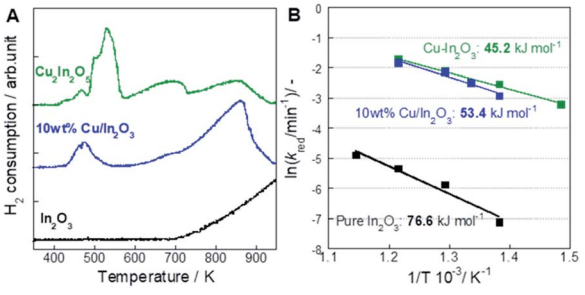

Fig. 5 Kinetics analysis of each oxide in the reduction step. (A) H_2-TPR profiles for Cu–In_2O_3 (derived from $Cu_2In_2O_5$), 10 wt% Cu/In_2O_3 and In_2O_3. (B) Arrhenius plots for the reduction of Cu–In_2O_3 (derived from $Cu_2In_2O_5$), 10 wt% Cu/In_2O_3 and In_2O_3.

Oxidation step by CO_2 for CO formation. Next, kinetics investigations were conducted for the oxidation step by CO_2 in the RWGS-CL cycle. The kinetics model for the oxidation of the oxide was also verified using the Hancock and Sharp method. As a consequence of the model fitting (details of which are presented in ESI Fig. S18–S21 and Tables S10–S12†), the most suitable models were concluded to be a zero-order model (R1 model)[25–27] for Cu–In_2O_3 and the nucleation model, known as the Avrami–Erofe'ev model (AE1 model), for the other two oxides.[28–30] Fig. 6A presents the Arrhenius plot for the oxidation of these three oxides. The reaction rate constant k values obtained from model fitting are presented in Table S13.† The activation energy for Cu–In_2O_3 is 50.7 kJ mol^{-1}, which is markedly lower than that for either of the other two oxides. As the results of the model fitting show, the large difference in the activation energy is attributable to the different mechanisms of oxidation among these oxides. Considering that AE1 is suitable as a model for In_2O_3 and 10 wt% Cu/In_2O_3, the overall oxidation of these two oxides is determined by the rate of formation and growth of the indium oxide nuclei. At the beginning of the reaction, the rate of oxidation is high because of random nucleation on the surface of the reduced oxide. However, as the nucleation and growth of nuclei proceed, the rate of oxidation plummets because of the decrease of the reduced surface. As a result, a long time is necessary to complete oxidation by CO_2. Fig. 6B presents different rates of CO_2 splitting over these oxides during oxidation by CO_2. For all oxides, the degree of reduction before re-oxidation was fixed at 3.0 mmol g^{-1}. On In_2O_3 and 10 wt% Cu/In_2O_3, the CO_2 splitting rate decreased drastically with the progress of oxidation. The oxidation of Cu–In_2O_3 proceeded while maintaining a constant CO_2 splitting rate of about 340 μmol g^{-1} min^{-1} until conversion reached 60%. As a result, re-oxidation of the reduced Cu–In_2O_3 is completed twice as rapidly as that of the other two oxides. These results obtained from the kinetics investigation of Cu–In_2O_3 suggest that the amount of active sites for CO_2 splitting remains constant while oxidation is proceeding. The oxidation state of the Cu–In_2O_3 surface during the oxidation step was analyzed by XPS. Compared with the In $3d_{5/2}$ peak of fully re-oxidized Cu–In_2O_3, that of reduced Cu–In_2O_3 was shifted to the lower binding energy (details in ESI Fig. S22 and ESI text†), which demonstrates the existence of In(0) species on the surface.[31] Fig. 6C shows the surface In/O ratio at each oxidation rate of the reduced Cu–In_2O_3 and 10 wt% Cu/In_2O_3, as measured by XPS. The In/O ratio of the Cu–In_2O_3 surface remained above 0.9, even at an oxidation rate of 75%, which indicates that bulk oxidation proceeds preferentially while the surface remains in a highly reduced state. This particular CO_2 splitting mechanism of Cu–In_2O_3 is explainable as shown in Fig. 6D. First, CO_2 splits on the surface of the Cu–In alloy; CO and oxide ions (O^{2-}) are generated. Subsequently, the O^{2-} ions migrate to the bulk of the

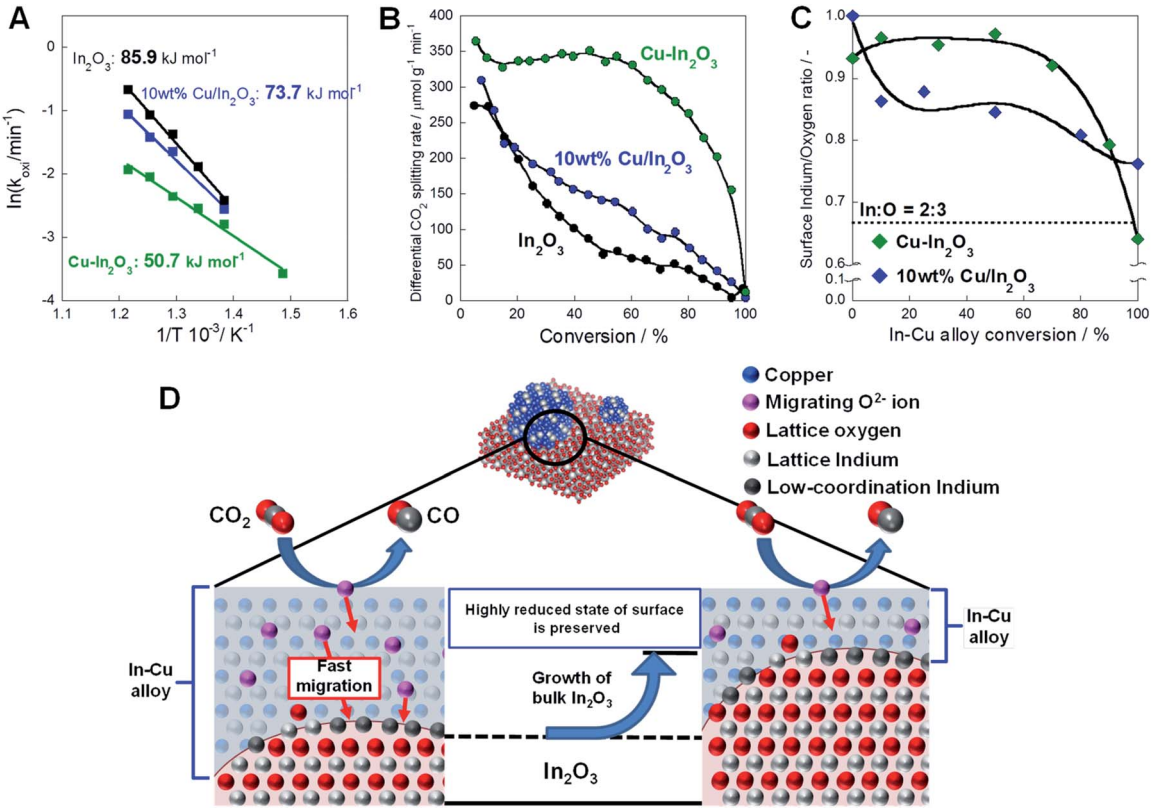

Fig. 6 Kinetics analysis of each oxide in re-oxidation steps. (A) Arrhenius plots for the oxidation of Cu–In_2O_3 (derived from $Cu_2In_2O_5$), 10 wt% Cu/In_2O_3 and In_2O_3. (B) Dependence of differential CO_2 splitting rate on conversion of oxides. (C) Surface In/O ratios on Cu–In_2O_3 and 10 wt% Cu/In_2O_3 during the re-oxidation step. (D) Presumed mechanism of CO_2 splitting on the reduced Cu–In_2O_3.

particle. They presumably oxidize the Cu–In alloy–In_2O_3 interface. As a result, the alloy surface, as the active site, remains in a highly reduced state. Rapid CO_2 splitting proceeds continuously.

Conclusion

As reported herein, Cu–In_2O_3 was synthesized. Then its performance for RWGS-CL was investigated at the low temperatures of 673–773 K. Results of RWGS-CL cycle tests demonstrated that, even at low temperatures, Cu–In_2O_3 exhibited much higher CO_2 splitting performance than ever reported. Results of XRD, STEM-EDX, and *in situ* XAFS measurements showed that the oxide has a structure of reduced Cu supported on In_2O_3 (Cu–In_2O_3) under the RWGS-CL conditions, and showed that its redox properties are based on Cu–In alloy formation and re-oxidation. In addition, because low performance was exhibited by pure In_2O_3 and Cu supported In_2O_3 that were prepared using an impregnation method, the structured state of Cu–In_2O_3 has extremely important roles in its high RWGS-CL performance. H_2-TPR and kinetics investigations revealed that Cu–In_2O_3 shows high reducibility, even at low temperatures. We concluded that Cu species promote the reaction of H_2 with the oxide surface. Results of kinetics investigations in the oxidation step indicate that the Cu–In alloy particle surface conserved a highly reduced state even under oxidation condition, resulting in rapid completion of re-oxidation by CO_2. The interesting oxidation behavior is attributed to rapid O^{2-} migration from the surface to the bulk of the Cu–In alloy and preferential oxidation of the interface of alloy–In_2O_3. The combination of high reducibility and the specific re-oxidation mechanism engenders the high performance found for RWGS-CL on Cu–In_2O_3.

Conflicts of interest

There are no conflicts to declare.

Acknowledgements

In situ XAFS measurements were performed at the beamline BL07 of the SAGA Light Source (Proposal No. 1910093P/BL07). The authors thank Dr H. Setoyama for help with measurements of XANES spectra.

Notes and references

1 *IPCC*, www.ipcc.ch/site/assets/uploads/2018/02/SYR_AR5_FINAL_full.pdf.
2 S. J. Davis, K. Caldeira and H. D. Matthews, *Science*, 2010, **329**, 1330–1333.

3 S. Perathoner and G. Centi, *ChemSusChem*, 2014, **7**, 1274–1282.
4 J. Artz, T. E. Müller, K. Thenert, J. Kleinekorte, R. Meys, A. Sternberg, A. Bardow and W. Leitner, *Chem. Rev.*, 2018, **118**, 434–504.
5 D. S. Mallapragada, N. R. Singh, V. Curteanu and R. Agrawal, *Ind. Eng. Chem. Res.*, 2013, **52**, 5136–5144.
6 F. V. Vázquez, J. Koponen, V. Ruuskanen, C. Bajamundi, A. Kosonen, P. Simell, J. Ahola, C. Frilund, J. Elfving, M. Reinikainen, N. Heikkinen, J. Kauppinen and P. Piermartini, *J. CO_2 Util.*, 2018, **28**, 235–246.
7 I. Dimitriou, P. García-Gutiérrez, R. H. Elder, R. M. Cuéllar-Franca, A. Azapagic and R. W. K. Allen, *Energy Environ. Sci.*, 2015, **8**, 1775–1789.
8 M. Romero and A. Steinfeld, *Energy Environ. Sci.*, 2012, **5**, 9234–9245.
9 P. Kaiser, R. B. Unde, C. Kern and A. Jess, *Chem. Ing. Tech.*, 2013, **85**, 489–499.
10 Y. A. Daza and J. N. Kuhn, *RSC Adv.*, 2016, **6**, 49675–49691.
11 K. Oshima, T. Shinagawa, Y. Nogami, R. Manabe, S. Ogo and Y. Sekine, *Catal. Today*, 2016, **232**, 27–32.
12 S.-C. Yang, S. H. Pang, T. P. Sulmonetti, W.-N. Su, J.-F. Lee, B.-J. Hwang and C. W. Jones, *ACS Catal.*, 2018, **8**, 12056–12066.
13 M. Wenzel, L. Rihko-Struckmann and K. Sundmacher, *AIChE J.*, 2017, **63**, 15–22.
14 Y. A. Daza, D. Maiti, R. A. Kent, V. R. Bhethanabotla and J. N. Kuhn, *Catal. Today*, 2015, **258**, 691–698.
15 D. Maiti, B. J. Hare, Y. A. Daza, A. E. Ramos, J. N. Kuhn and V. R. Bhethanabotla, *Energy Environ. Sci.*, 2018, **11**, 648–659.
16 L. Ma, Y. Qiu, M. Li, D. Cui, S. Zhang, D. Zheng and R. Xao, *Ind. Eng. Chem. Res.*, 2020, **59**, 6924–6930.
17 Y. Qiu, L. Ma, D. Zeng, M. Li, D. Cui, Y. Lv, S. Zhang and R. Xiao, *J. Energy Chem.*, 2020, **46**, 123–132.
18 D. Zeng, Y. Qiu, L. Ma, M. Li, D. Cui, S. Zhang and R. Xiao, *Environ. Sci. Technol.*, 2020, **54**, 12467–12475.
19 N. Utsis, M. V. Landau, A. Erenburg and M. Herskowitz, *Catalysts*, 2020, **10**, 1082.
20 X. Zhu, K. Li, L. Neal and F. Li, *ACS Catal.*, 2018, **8**, 8213–8236.
21 Z. Bahari, E. Dichi, B. Legendre and J. Dugué, *Thermochim. Acta*, 2003, **401**, 131–138.
22 M. G. Kim, S. Sim and J. Cho, *Adv. Mater.*, 2010, **22**, 5154–5158.
23 W.-R. Lee, M. G. Kim, J.-R. Choi, J.-I. Park, S. J. Ko, S. J. Oh and J. Cheon, *J. Am. Chem. Soc.*, 2005, **127**, 16090–16097.
24 K. Ploner, L. Schlicker, A. Gili, A. Gurlo, A. Doran, L. Zhang, M. Armbrüster, D. Obendorf, J. Bernardi, B. Klötzer and S. Penner, *Sci. Technol. Adv. Mater.*, 2019, **20**, 356–366.
25 J. D. Hancock and J. H. Sharp, *J. Am. Ceram. Soc.*, 1972, **55**, 74–77.
26 K. Piotrowski, K. Mondal, H. Lorethova, L. Stonawski, T. Szymański and T. Wiltowski, *Int. J. Hydrogen Energy*, 2005, **30**, 1543–1554.
27 Z. Zhou, L. Han and G. M. Bollas, *Int. J. Hydrogen Energy*, 2014, **39**, 8535–8556.
28 M. Avrami, *J. Chem. Phys.*, 1939, **7**, 1103–1112.
29 M. Avrami, *J. Chem. Phys.*, 1940, **8**, 212–224.
30 M. Avrami, *J. Chem. Phys.*, 1941, **9**, 177–184.
31 J. Gao, F. Song, Y. Li, W. Cheng, H. Yuan and Q. Xu, *Ind. Eng. Chem. Res.*, 2020, **59**, 12331–12337.